
# Particle modelling in biomass combustion using orthogonal collocation

Applied Energy 255 (2019) 113868

Contents lists available at ScienceDirect

Applied Energy

journal homepage: www.elsevier.com/locate/apenergy

# Particle modelling in biomass combustion using orthogonal collocation

Maulana G. Nugraha[a], Harwin Saptoadi[b], Muslikhin Hidayat[c], Bengt Andersson[a], Ronnie Andersson[a,*]

[a] Department of Chemistry and Chemical Engineering, Chalmers University of Technology, SE-41296 Gothenburg, Sweden
[b] Department of Mechanical and Industrial Engineering, Universitas Gadjah Mada, Yogyakarta 55281, Indonesia
[c] Department of Chemical Engineering, Universitas Gadjah Mada, Yogyakarta 55281, Indonesia

## HIGHLIGHTS

- Physicochemical particle model for drying, devolatilization and combustion.
- Highly accurate and stable model providing good agreement with experimental data.
- Continuous profiles of temperature and biomass component during conversion.
- Computationally efficient model easy to implement in CFD analysis.

## GRAPHICAL ABSTRACT

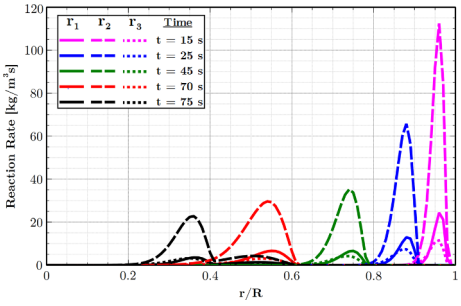


## ARTICLE INFO

*Keywords:*
Biomass combustion
Biomass pyrolysis
Particle model
Orthogonal collocation
Stefan flow

## ABSTRACT

Development of an accurate and computational efficient biomass particle model to predict particle pyrolysis and combustion is the focus of this paper. Partial differential equations (PDEs) for heat and mass balance are transformed into a system of coupled ordinary differential equations (ODEs) with the use of orthogonal collocation as the particle discretization method. The orthogonal collocation method is incorporated with comprehensive physicochemical mechanisms to predict the behavior of biomass components during particle pyrolysis and combustion. Heat adsorption by evaporated gas and water movement by diffusion inside the biomass matrix are included in the present work, in parallel with the effect of Stefan flow on the heat and mass transfer rates at the particle surface. Abandoning the classical interface-based modelling approach, the present approach allows decoupling between biomass components and spatial resolution, and the prediction of continuous intra-particle profiles.

The new particle model is proven to be accurate and stable through its high degree of agreement with simulation results for particle pyrolysis and combustion experiments using different particle moisture contents and geometrical shapes. The intra-particle temperature gradient, as well as particle mass and size evolution, can be predicted accurately, as validated against experimental data. It is shown that six collocation points provide satisfying resolution. The computational efficiency is confirmed by the short simulation time that was found to be approximately three orders of magnitude faster than mesh-based simulations. This implies that the current model can be used for computational fluid dynamic (CFD) analysis through implementation as sub-grid-scale models to design, for example, biomass furnaces.

* Corresponding author.
*E-mail address:* ronnie.andersson@chalmers.se (R. Andersson).

https://doi.org/10.1016/j.apenergy.2019.113868
Received 14 February 2019; Received in revised form 14 August 2019; Accepted 5 September 2019
Available online 11 September 2019

**Nomenclature**

| | |
|---|---|
| $A$ | pre-exponential factor [$s^{-1}$]; orthogonal collocation coefficient for first derivative [-] |
| $A_p$ | particle surface area [$m^2$] |
| $B$ | orthogonal collocation coefficient for second derivative [-] |
| $Bi$ | Biot number [-] |
| $B_M$ | correction factor for Sherwood number due to Stefan flow [-] |
| $B_T$ | correction factor for Nusselt number due to Stefan flow [-] |
| $Cp$ | specific heat capacity [J $kg^{-1}$ $K^{-1}$] |
| $d$ | orthogonal collocation coefficient |
| $d_{pore}$ | particle pore diameter [m] |
| $D$ | diffusivity [$m^2$ $s^{-1}$] |
| $D_p$ | diameter particle [m] |
| $E_a$ | activation energy [kJ $mol^{-1}$] |
| $h$ | convective heat transfer coefficient [W $m^{-2}$ $K^{-1}$] |
| $h_m$ | convective mass transfer coefficient [m $s^{-1}$] |
| $k$ | reaction rate constant [$s^{-1}$] |
| $l$ | thickness [m] |
| $L$ | length [m] |
| $Le$ | Lewis number [-] |
| $\dot{m}$ | mass flow rate [kg $m^{-2}$ $s^{-1}$] |
| $M$ | molecular weight [kg $kmol^{-1}$] |
| $N$ | total collocation points [-] |
| $Nu$ | Nusselt number [-] |
| $Pr$ | Prandtl number [-] |
| $r$ | local radius [m] |
| $\dot{r}$ | reaction rate [kg $m^{-3}$ $s^{-1}$] / [kg $m^{-2}$ $s^{-1}$] |
| $R$ | radius [m]<br>ideal gas constant [kJ $mol^{-1}$ $K^{-1}$] |
| $Re$ | Reynold number [-] |
| $Sh$ | Sherwood number [-] |
| $Sc$ | Schmidt number [-] |
| $S$ | mass source term of gas [kg $m^{-3}$ $s^{-1}$] |
| $t$ | time [s] |
| $T$ | temperature [K] |
| $u$ | velocity [m $s^{-1}$] |
| $V$ | volume [$m^3$] |
| $W$ | width [m] |
| $x$ | dimensionless coordinate [-] |
| $Y_i$ | gas species mass fraction [-] |

*Greek letters*

| | |
|---|---|
| $\Delta H$ | heat of reaction [kJ $kg^{-1}$] |
| $a$ | geometry coefficient [-] |
| $\beta$ | shrinking and swelling factor [-] |
| $\varepsilon$ | porosity [-] |
| $\lambda$ | thermal conductivity [W $m^{-1}$ $K^{-1}$] |
| $\rho$ | density or species concentration [kg $m^{-3}$] |
| $\sigma$ | Emissivity [-] |
| $\omega$ | Stefan-Boltzmann constant [W $m^{-2}$ $K^{-4}$] |

*Subscript*

| | |
|---|---|
| 0 | initial or original |
| *ash* | ash |
| *b* | dry biomass |
| *tot* | cumulative properties for biomass |
| *bulk* | bulk gas |
| *bw* | bound water |
| *c* | char |
| *char* | char reaction |
| $CO_2$ | carbon monoxide |
| *dev* | devolatilization |
| *dry* | drying |
| *eff* | effective properties |
| *fw* | free water |
| *g* | gas |
| $H_2O$ | water vapor |
| *i* | index for reaction or collocation point location, index of gas species |
| *j* | index for Euclidean point |
| *k* | index for species or reaction |
| $O_2$ | oxygen |
| *p* | particle |
| *s* | area based (for reaction) |
| *surf* | particle surface |
| *v* | volume based (for reaction) |
| *wall* | reactor wall |

## 1. Introduction

The rising demand for the worldwide energy and the worldwide concern for global warming due to $CO_2$ emission has accelerated global interest in alternative energy conversion from biomass [1,2]. Various biomass-type conversions into sustainable heat and power, from dedicated crops to solid biomass waste, via the combustion process, are at the center of scientific and industrial focus today [3].

One of the challenges in this research area is the design of efficient and low emission furnaces, which calls for the development of computationally efficient mathematical models that accurately describe complex physicochemical phenomena including biomass drying, devolatilization, and combustion. Material properties and particle size determine whether the particles are thermally thin or thick, and thereby determine the level of mathematical modelling complexity needed to accurately describe the phenomena. Significant model simplification is achieved for thermally thin particles due to temperature uniformity throughout the particle [4,5]. However, for thermally thick particles, the non-uniform temperature profile inside the particle cannot be neglected. The temperature non-uniformity also means that the conversion stages, i.e. drying, devolatilization, and char combustion, occur simultaneously and also change over time. Obviously only modelling approaches that allow space and time resolution are suitable under these conditions. The formal classification of particles as either thick or thin is given by the thermal Biot number as presented in Eq. (1). A particle with Biot number lower than 0.1 is considered as a thermally thin particle while a particle with a higher Biot number is categorized as thermally thick [6,7].

$$Bi = \frac{h_{eff}\, d}{\lambda} \tag{1}$$

Two different particle discretization approaches have been used by researchers to model thermally thick biomass particle combustion, i.e. mesh-based discretization [8–15] and interface-based discretization [7,16–22]. Mesh-based models rely on numerical discretization, which divides each particle into several grid points and directly solves all governing equations in each grid point, as illustrated in Fig. 1 [23]. In contrast, the interface-based model relies on a discretization scheme that divides a particle into layers based on available biomass component mass, and how these change in time, as described in Fig. 2. The layers can be composed of either moist and dry biomass, char, or ash [16].

Both aforementioned discretization methods have their own advantages and limitations in terms of numerical efficiency, accuracy, and

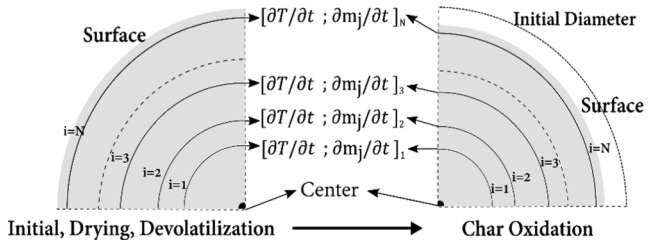


**Fig. 1.** Mesh-based particle discretization scheme.

stability. The mesh-based discretization allows the highest accuracy since it provides resolution of intra-particle profiles and the simultaneous existence of biomass components, which can be maintained. This discretization method, thereby, allows detailed resolution of the complex phenomena occurring inside single particles, which could not be handled by the interface discretization model [23].

The accuracy of this model requires the utilization of a fine computational grid. However, this leads to a substantial increase in computational resources as more equations must be solved in each time step, as shown in Fig. 1. As reported in previous publications, the simulation times can vary from several minutes [10] up to an hour [15] to simulate the combustion of one single thermally thick particle using the mesh-based discretization scheme. Therefore, it is not feasible to use this discretization to simulate a large number of biomass particles in a real stove or furnace, particularly if it needs to be coupled with external flow and temperature fields, such as in computational fluid dynamic (CFD) analysis. A CFD analysis requires the formulation and transformation of the PDEs into a system of ordinary differential equations.

The interface-based model is superior in terms of computational efficiency compared to the mesh-based model. The superiority arises in that the total number of equations that must be solved using the interface-based model are much fewer than the mesh-based model, as described in Fig. 2. The ability to integrate the interface model in a CFD environment and couple the solution to an external flow field has been demonstrated in different studies [7,17,21,22,24].

However, from a numerical solution accuracy point of view, the interface-based simulation has an issue with discontinuities that occur when layers disappear. The disappearance of each particle layer has also been found to lead to numerical instabilities in particle behavior prediction [21]. Based on the lumped formulation, intra-particle profile and material properties are described in a few discrete points, which do not fully represent the real profiles and may lead to a decrease in accuracy [23]. As such, the method is confined by an inherent limitation in resolution and cannot be enhanced by adding more layers since this discretization method depends on pre-defined biomass components. A step-function of the reaction region inside the particle is the main source of discontinuity at the location of the reaction front [17].

The present study presents a new computationally efficient scheme for particle discretization that accommodates the accurate prediction of single-particle biomass pyrolysis and combustion. Orthogonal collocation is employed, which has been widely used to solve different problems for heat and mass transfer along with chemical reactions in various engineering applications [25–33].

The main advantages of the orthogonal collocation approach include the improved prediction of intra-particle profiles, the ability to decouple resolution from biomass components, and it also allows parallel reactions to be handled as the mesh-based model while maintaining a sufficiently low computational effort. The utilization of orthogonal collocation also allows improvement on heat and mass transfer prediction inside a particle and at the particle surface. Some additional important physicochemical phenomena included in the mathematical formulation in this paper are i.e. the movement of free and bound water by diffusion, heat exchange between phases, and correction of heat and mass transfer rates at the particle surface due to Stefan flow. The transformation of governing PDEs for heat and mass balance into a system of ODEs with the use of orthogonal collocation also allows the current model to be implemented further in the CFD environment using sub-grid-scale modelling due to its computational efficiency. However the narrow reaction zone moving through the particle may produce uneven release of pyrolytic gases and water vapor if the space resolution is not high enough. Since uneven reaction rate cause challenges to obtain convergence CFD simulations, this study also focuses on understanding how to achieve even reaction rates while maintaining computational efficiency. An overview of the different discretization methods that handle specific physical phenomena and applications is presented in Table 1.

The present study contributes to the simulation methods for biomass combustion by introducing a new particle discretization method and by validating the model with the experimental data presented in the literature. Additional testing of numerical accuracy, efficiency, and stability was also conducted to measure how robust the proposed model was in predicting single biomass particle pyrolysis and combustion behavior.

## 2. Model description

### 2.1. Biomass decomposition

#### 2.1.1. Drying

Water is present as bound water, free water, and water vapor inside a biomass matrix. Water is first taken up as bound water until all available adsorption sites have been occupied, and then it becomes free water that fills biomass pores [34]. The limit on bound water that can

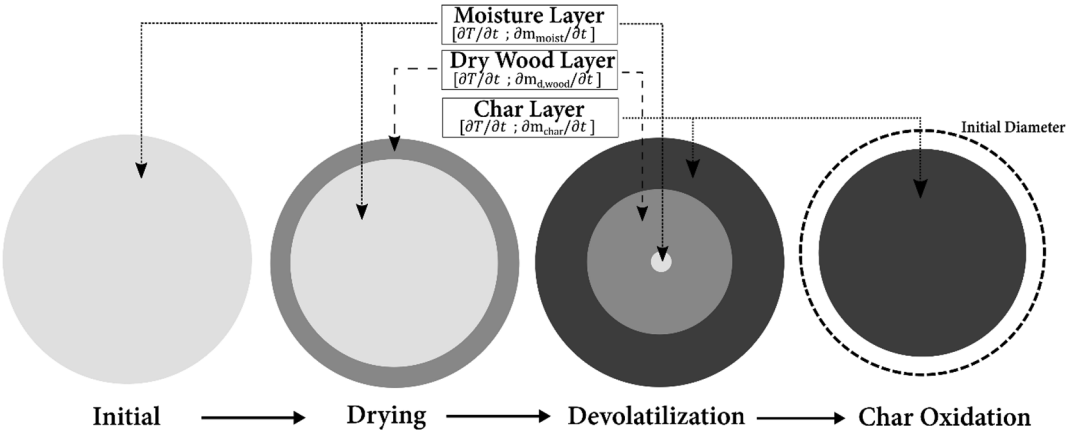


**Fig. 2.** Interface-based particle discretization scheme.

**Table 1**
Conceptual overview of discretization methods with regard to different physical phenomena.

| Physical phenomena | Mesh | Interface | Collocation |
|---|---|---|---|
| Decoupling species and space resolution | + + | − | + + |
| Smooth species profile | + + | − | + |
| Water transport inside particle due to diffusion | + + | − | + + |
| Distinction of bound and free water | + + | * | + + |
| Heat exchange between solid and evaporated gas | + + | + + | + + |
| Consecutive gas reaction occurred inside particle, i.e. secondary devolatilization | + + | − | + + |
| Stefan flow effect | * | * | + + |
| Particle shrinking and swelling during drying, devolatilization, and char reaction | + + | + + | + + |
| Easy implementation as sub-grid models for CFD analysis (multi particle and furnace) | − | + + | + |

(+ +) high degree of agreement; (+) good agreement; (−) disagreement; *possible to be implemented.

be present in the biomass matrix, i.e. the fiber saturation point (FSP), depends on the material, but it has an average value that is around 30 wt% on dry basis [35].

Free and bound water may move inside a particle due to capillary forces and concentration gradient by diffusion. Upon heating, due to evaporation, both bound and free water transform into the gas phase as water vapor [23]. Free and bound water have different characteristics with respect to transport and evaporation, which implies that these two different forms of water must be treated carefully [12].

The drying process is modelled with three different approaches in literatures, i.e. equilibrium, heat sink (thermal drying), and Arrhenius (kinetic rate) models [23,36]. The equilibrium model is useful for predicting low-temperature drying conditions, e.g. drying wood for building materials. The heat sink (thermal drying) model relies on step-function evaporation, which can lead to numerical instabilities. The kinetic rate model is used in the present study due to its wide range of temperature applications and high numerical stability, both of which can increase simulation robustness and accuracy for fast drying conditions [15].

### 2.1.2. Devolatilization

Pyrolysis and devolatilization are terms used interchangeably and refer to the thermochemical degradation process of biomass in absence of an oxidizer [12]. Up to 90% of solid particle mass is converted into pyrolytic gas during this process [37]. The different release stages of pyrolytic volatiles divide the devolatilization process into primary and secondary devolatilization where various parallel and consecutive reactions occur [38]. Biomass is decomposed into volatile gas, primary tars, and char during the primary devolatilization which is considered to be an endothermic reaction that is completed at relatively low temperatures (below 773 K) [39]. While secondary devolatilization occurs during the outward transport of primary tars. In this period, primary tars participate in various complex reactions such as cracking, reforming, dehydration, condensation, polymerization, oxidation, and gasification [17]. Meanwhile, secondary devolatilization can be neglected due to its insignificant effect on a simulation [40]. This simplification of secondary devolatilization is linked to the assumption that produced gases exit the biomass particle immediately after it have been devolatilized [7,16,18,20]. This is valid assumption for combustion and pyrolysis cases when the ratio between the residence time of the volatile gas and the reaction time of secondary devolatilization is small.

The Arrhenius kinetic rate model is commonly used in particle modelling to describe the devolatilization process. However, different reaction schemes have been proposed in the literature with varying degrees of complexity. The first and the simplest devolatilization model is referred to as a one-step global model, and it describes biomass decomposition into volatile gas, char, and tar using a single reaction. The second model, which has been widely used, includes three independent competitive reactions. The solid material is converted competitively into volatile gas, tar, and char [7,9–11,19,34,41,42]. Alternatively, more complex devolatilization mechanisms may be used, including mechanisms based on the three main pseudo components in the biomass (cellulose, hemicellulose, and lignin), which are converted into volatile gas species, tar, and char. Fig. 3 illustrates the differences among these three models.

Each devolatilization model has its own advantages and disadvantages and requires the specification of the pre-exponential coefficients and activation energies for the different reactions. In addition, compared with the last two schemes, the implementation of the global model also requires knowledge about the distribution coefficients (α, β and γ) of each product formed as these are not embedded in the model as they are in the second scheme. The third model has the advantage of broad prediction of volatile species, which makes the prediction of the composition of pyrolytic gas possibly even more accurate [21,43]. Moreover, it can be applied for various types of biomass in which the composition of the three main pseudo components is known. This model allows temperature dependent decomposition rates of the lignin, hemicellulose and cellulose, but it also requires definitions of the share of gases and char in order to allow improved predictions of the composition of pyrolytic gas. However, compared with the first and second model, the third model must handle more equations to track the evolution of each pseudo components. Increased computational cost is necessary to utilize the pseudo-components-based-model [23]. However, the proposed particle simulation method allows arbitrary schemes to be used.

### 2.1.3. Char oxidation and gasification

The last stage of biomass combustion is heterogeneous char reaction, which involves the reaction of remaining solid carbon (char) with oxidative gases. The simplification of char oxidation and gasification as used in the present study follows the reaction scheme below: [12]

$$C + O_2 \xrightarrow{k_4} CO_2$$

$$C + CO_2 \xrightarrow{k_5} 2CO$$

$$C + H_2O \xrightarrow{k_6} CO + H_2$$

The char conversion rate is controlled by a series of transport mechanism solid-gas reactions [44]: (1) film diffusion of an oxidizing agent, (2) diffusion through the ash layer and particle, (3) adsorption onto the reaction surface, (4) chemical reaction, (5) desorption of product gas from the surface, (6) diffusion of product gas through the particle and the ash layer, and (7) film diffusion back into the ambient

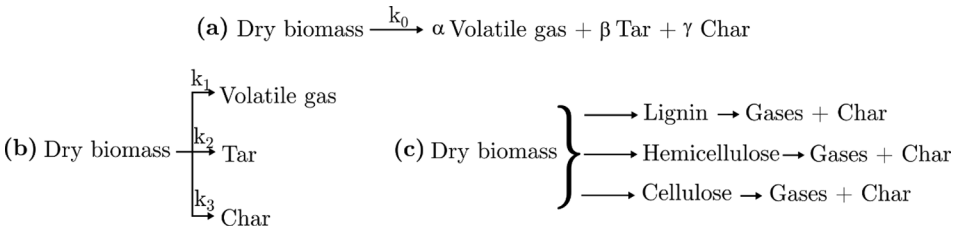


**Fig. 3.** Biomass devolatilization schemes (a) one-step global model (b) three independent competitive reaction models (c) three main pseudo components.

gas. Except for the chemical reaction (step number 4), the remaining steps are mass transport. Based on the Thiele modulus (the ratio of the overall reaction rate to diffusion rate) and the effectiveness factor [45], three different regimes of char conversion can be present in a system, depending on if the reaction takes place inside the particle, at the particle surface, or at both locations. The most influential factor determining the reaction location is the balance between mass transfer and reactions rates, which strongly depends on the temperature [45].

### 2.2. Model formulation and governing equations

The governing equations and constitutive relationships are summarized in Table 2 and Table 3. The following assumptions were made in formulating the model for biomass pyrolysis and combustion:

1) 1D-transient simulation is employed to predict the evolution of particle.
2) Gas phase follows the ideal gas law, and its fluid properties are pressure and temperature dependent.
3) The transport of evaporated gas from the biomass matrix is fast, and the second stage of devolatilization does not occur inside the particle.
4) Gas phase is in thermal equilibrium with the local solid phase while transported out, because the heat capacity of the gases is high compared to the heat of devolatilization. This heat transfer has a significant effect on simulation accuracy [23].
5) Particle shrinking only occurs during char oxidation and gasification.
6) Char oxidation occur at the particle surface considering the size of the simulated particle and the high reaction temperature. This is supported experimentally by Karlström et al. [46], who used an 8 mm diameter wood particle and found that external oxygen diffusion is the limiting step of the reaction.
7) The ash layer has high permeability and does not cause any significant mass transfer resistance.
8) The heat capacity of gas in the accumulation term is neglected due to the insignificant density of gas.

The global energy conservation equation for 1D-transient simulation follows from Eq. (2). In Eq. (2), $a$ depends on particle geometry (0 for planar, 1 for cylinder, and 2 for sphere). The term on the left side of Eq. (2) corresponds to the accumulated heat. The first term on the right side in Eq. (2) describes Fourier heat conduction, the second term refers to local heating of evaporated gas, the third term refers to the heat exchange due to the mobility of free and bound water, and the last two terms represent the heat sink due to drying and endothermic devolatilization reaction. The boundary condition for heat balance at the particle surface follows Eq. (3). The heat conduction into a particle is balanced with heat transfer to or from the particle due to convective and radiative heat transfer and also due to the exothermic char reaction that occurs at the particle surface.

The mass evolution of dry biomass, char, free water, and bound water follows the expressions from Eqs. (4)–(7). The current model allows the movement of free and bound water inside a biomass matrix by diffusion, which is represented by the first term on the right-hand side in Eqs. (6) and (7). While the last term on the right-hand side of Eqs. (4)–(7) allows control of the density of species due to particle shrinking or swelling.

The evolution of the particle porosity is given by Eq. (8). This allows the current model to determine how the macroscopic material properties, for example the effective thermal conductivity, change at different locations as function of time due to changes in temperature, biomass component composition and porosity, as given by Eq. (12).

Evolution of particle volume due to shrinking and swelling that take place during drying, pyrolysis, and char reaction is expressed in Eq. (9). In Eq. (9), $\beta_m$ and $\beta_b$ are the swelling or shrinking factors for drying and devolatilization, respectively. As mentioned above, it is assumed that the shrinkage of a particle only occurs due to char oxidation and gasification, hence, the first two terms on the right side of Eq. (9) are neglected in the present simulation. These two terms are neglected because of the lack of quantitative information and evidence of particle evolution during drying and devolatilization in the current experimental data sets [12].

The gas phase continuity equation and gas phase components conservation equation, in Eqs. (10)–(11), are important to be included especially when secondary devolatilization occur in the particle [12]. Gas species conservation equations are derived based on the convective and diffusive transport inside the biomass matrix and the source term which allows the reaction that occur inside the particle to be accounted for. However, Eqs. (10) and (11) were not included in present simulation work due to the third assumption that is stated in the beginning of this section.

$$\frac{\partial \varepsilon \rho_g}{\partial t} + \frac{1}{r^a}\frac{\partial}{\partial r}(r^a \varepsilon \rho_g u) = S_g \tag{10}$$

$$\frac{\partial}{\partial t}\varepsilon \rho_g Y_i + \frac{1}{r^a}\frac{\partial}{\partial r}(r^a \varepsilon \rho_g Y_i u) = \frac{1}{r^a}\frac{\partial}{\partial r}(r^a D_{eff,i} \varepsilon \rho_g)\frac{\partial Y_i}{\partial r} + S_i \tag{11}$$

Additional supporting equations for heat and mass balances are listed in Table 3. The effective thermal conductivity in Eq. (12), which is constructed from a theoretical basis [47,48] and with empirical verification [49], is calculated as the summation of conductive and radiative components. Moreover, the presented form of effective thermal conductivity in Eq. (12) has been widely used in biomass particle combustion modelling and has been found to produce good agreement with experimental data [12,14,15,37].

**Table 2**
Governing equations.

| | | |
|---|---|---|
| Temperature | $\sum \rho_k Cp_k \frac{\partial T}{\partial t} = \frac{1}{r^a}\frac{\partial}{\partial r}(r^a \lambda_{eff})\frac{\partial T}{\partial r} - \dot{r}_{v,g} Cp_g \frac{V_p}{A_p}\frac{\partial T}{\partial r} + \left(D_{fw} Cp_{fw}\frac{d\rho_{fw}}{dr} + D_{bw} Cp_{bw}\frac{d\rho_{bw}}{dr}\right)\frac{dT}{dr} - \Delta H_{dry}\dot{r}_{v,dry} - \Delta H_{dev}\dot{r}_{v,dev}$ | (2) |
| Boundary condition (temperature) | $\lambda_{eff}\frac{\partial T}{\partial r} = h_{eff}(T_{bulk} - T_{surf}) - \sigma\omega(T_{surf}^4 - T_{wall}^4) - \Delta H_{char}\dot{r}_{s,char}$ | (3) |
| Dry biomass density | $\frac{\partial \rho_b}{\partial t} = -\dot{r}_{v,dev} - \frac{\rho_b}{V}\frac{dV}{dt}$ | (4) |
| Char density | $\frac{\partial \rho_c}{\partial t} = k_3 \rho_w - \frac{\rho_c}{V}\frac{dV}{dt}$ | (5) |
| Free water density | $\frac{\partial \rho_{fw}}{\partial t} = \frac{1}{r^a}\frac{\partial}{\partial r}(r^a D_{fw})\frac{\partial \rho_{fw}}{\partial r} - k_4 \rho_{fw} - \frac{\rho_{fw}}{V}\frac{dV}{dt}$ | (6) |
| Bound water density | $\frac{\partial \rho_{bw}}{\partial t} = \frac{1}{r^a}\frac{\partial}{\partial r}(r^a D_{bw})\frac{\partial \rho_{bw}}{\partial r} - k_5 \rho_{bw} - \frac{\rho_{bw}}{V}\frac{dV}{dt}$ | (7) |
| Porosity | $\frac{\partial \varepsilon}{\partial t} = -\left(\frac{\partial \rho_b}{\partial t} + \frac{\partial \rho_c}{\partial t} + \frac{\partial \rho_{fw}}{\partial t} + \frac{\partial \rho_{bw}}{\partial t}\right) \times \frac{(1-\varepsilon)}{\rho_{tot}} + \frac{(1-\varepsilon)}{V}\frac{dV}{dt}$ | (8) |
| Volume | $\frac{dV}{dt} = \frac{V_0(\beta_m - 1)}{\rho_{fw_0} + \rho_{bw0}}\dot{r}_{v,dry} + \frac{V_0(\beta_b - 1)}{\rho_{b0}}\dot{r}_{v,dev} + \frac{A_p \dot{r}_{s,char}}{\rho_{tot}}$ | (9) |

**Table 3**
Supporting equations for main heat and mass balance.

| | | |
|---|---|---|
| Thermal conductivity | $\lambda_{eff} = \frac{\varepsilon\sigma T^3 d_{pore}}{\omega} + \varepsilon\lambda_g + (1-\varepsilon)((x_b + x_{fw} + x_{bw})\lambda_b + x_c\lambda_c + x_{ash}\lambda_{ash})$ | (12) |
| Bound water diffusivity | $D_{bw} = 1.05 \times 10^{-5}\exp\left(\frac{-4633 + 3523\frac{\rho_{bw}}{\rho_{tot}}}{T}\right)$ | (13) |
| Devolatilization rate | $\dot{r}_{v,dev} = (k_1 + k_2 + k_3)\rho_b$ | (14) |
| Drying rate | $\dot{r}_{v,dry} = k_4\rho_{fw} + k_5\rho_{bw}$ | (15) |
| Char oxidation rate | $\dot{r}_{s,char} = (k_{6,eff} \times C_{O_2} + k_{7,eff} \times C_{CO_2} + k_{8,eff} \times C_{H_2O}) \times M_c$ | (16) |
| Effective char reaction rate constant (for reaction index 4–6) | $k_{i,eff} = \frac{k_i h_{m\_eff,i}}{k_i + h_{m\_eff,i}}$ | (17) |
| Kinetic rate constant | $k_i = A_i\exp\left(\frac{-E_{a,i}}{R_g T}\right)$ | (18) |
| Gas production rate | $\dot{r}_{v,g} = \dot{r}_{v,dry} + (k_1 + k_2)\rho_b$ | (19) |
| Convective mass transfer coefficient | $h_{m,i} = \frac{D_g Sh_{eff}}{D_p}$ | (20) |
| Effective convective mass transfer coefficient | $h_{m\_eff,i} = \frac{h_{m,i} D_g \varepsilon_{ash}}{l_{ash}\left(h_{m,i} + \frac{D_g}{l_{ash}}\right)}$ | (21) |
| Ash layer thickness | $l_{ash} = \frac{\rho ash_0}{\rho_{tot0}} \times \frac{1}{a+1} \times \left(\frac{r_0^{a+1} - r^{a+1}}{r_0^a - r^a}\right)$ | (22) |
| Effective convective heat transfer coefficient | $h_{eff} = \frac{Nu_{eff}\lambda_g}{D_p}$ | (23) |

The liquid free water diffusivity ($D_{fw}$) is taken from the work by Souza and Nebra [50], which allows the calculation of effective diffusivity based on free water concentration and local temperature. Meanwhile, the bound water diffusivity, follows Eq. (13) [51].

The reaction kinetics of drying, devolatilization, and char reactions in Eqs. (14), (15), and (17) follow the Arrhenius equation in Eq. (18). The effective reaction rate should be used to calculate the total char reaction rate and account for the mass transfer limitation of oxygen, as shown by Eq. (16). The gas formation is due to water evaporation and the decomposition of dry biomass into tar and volatile gas, as presented in Eq. (19).

The convective mass transfer coefficient used to calculate the effective char reaction rate may be corrected from its original form, in Eqs. (20) to Eq. (21) due to the presence of an ash layer. The thickness of the ash layer follows Eq. (22). However detailed information on ash is not available; it is considered to be permeable, causing negligible transport resistance, and is therefore neglected in the proceeding analysis.

The effective convective heat transfer coefficient used in the calculation of the boundary condition for heat transfer in Eq. (3) follows Eq. (23). The Nusselt and Sherwood numbers should be corrected due to the net flow from the boundary layer, i.e. the effect of the Stefan flow. The nominal correlations for the Nusselt and Sherwood numbers prior to correction for the Stefan flow are summarized in Table 4 for different particle geometries.

The effective Sherwood and Nusselt numbers in the present simulation work, are calculated using Michaelides correlations in Eqs. (30) and (31) [53].

$$Sh_{eff} = \frac{Sh}{(1 + B_M)^{0.7}} \tag{30}$$

$$Nu_{eff} = \frac{Nu}{(1 + B_T)^{0.7}} \tag{31}$$

$B_M$ and $B_T$in Eqs. (30) and (31) are calculated using Eqs. (32) and (33).

$$B_M = exp\left(-\frac{\dot{m}_{s,g} R}{D_g \rho_g}\right) - 1 \tag{32}$$

$$B_T = (1 + B_M)^{\frac{Cp_g}{Cp_{bulk}\,Le}} - 1 \tag{33}$$

### 2.3. Discretization by orthogonal collocation

Discretization using the orthogonal collocation method was utilized in order to solve the governing equations in Section 2.2. The method discretizes the finite-sized biomass particle into several collocation points and solves the governing equations for each collocation point.

The discretization scheme looks similar to numerical discretization, which uses the mesh-based model. The main difference between the methods is in the expansion of differential terms in the governing equations. The mesh-based model uses a backward, forward, or central differentiation scheme, which only utilizes the adjacent grid points to calculate an observed point. Meanwhile, the orthogonal collocation method uses all values from all collocation points to calculate value at an observed point. This leads to a significant reduction of employed points to achieve mesh independence result, as presented in this paper. In comparison, many more grid points are typically needed by the ordinary mesh-based model to solve one-dimensional particle combustion and pyrolysis problems [15,37,54].

The solution of the dependent variable was expanded using orthogonal polynomials as the trial function, and for this present work the shifted Legendre orthogonal polynomial was utilized. The expanded solution of temperature at a collocation point follows Eq. (34), in which $N$ is the total number of collocation points [55].

$$T(x_j) = \sum_{i=1}^{N+1} d_i x_j^{2i-2} \tag{34}$$

The first and second derivatives of the polynomial function in Eq.

**Table 4**
Supporting equations for main heat and mass balance.

| | | | | |
|---|---|---|---|---|
| Spherical [14,21] | $Nu = 2 + 0.6Re^{0.5}Pr^{1/3}$ | (24) | $Sh = 2 + 0.6Re^{0.5}Sc^{1/3}$ | (25) |
| Cylindrical [52] | $Nu = (0.4Re^{0.5} + 0.6Re^{2/3})Pr^{0.4}$ | (26) | $Sh = (0.4Re^{0.5} + 0.6Re^{2/3})Sc^{0.4}$ | (27) |
| Planar [12] | $Nu = 0.644Re^{0.5}Pr^{0.343}$ | (28) | $Sh = 0.644Re^{0.5}Sc^{0.343}$ | (29) |

**Table 5**
Experimental conditions from Lu et al. [12]

| Experiment condition | Case A | Case B | Case C | Case D |
|---|---|---|---|---|
| Wall temperature (K) | 1276 | 1276 | 1276 | 1276 |
| Gas temperature (K) | 1050 | 1050 | 1050 | 1050 |
| Initial moisture content (wt%) | 6 | 6 | 40 | 40 |
| Gas material | Nitrogen | Nitrogen | Nitrogen | Air |
| Particle shape | Sphere | Cylinder | Cylinder | Sphere |
| Particle material | Poplar | Poplar | Poplar | Poplar |
| Particle diameter (mm) | 9.5 | 9.5 | 9.5 | 9.5 |

(34) follows Eqs. (35) and (36).

$$\frac{dT}{dx}(x_j) = \sum_{i=1}^{N+1} d_i (2i-2) x_j^{2i-3} \tag{35}$$

$$\frac{d^2T}{dx^2}(x_j) = \sum_{i=1}^{N+1} d_i (2i-3)(2i-2) x_j^{2i-4} \tag{36}$$

The solution in a particular collocation point can be combined together with the solution from another points to produce a global solution matrix. By rearranging the matrix form of global solution, the substitution of the unknown$d_i$ at a collocation point can be performed. This substitution produces $N+1$ number of unknown $(x_j)$, which can be solved using $N+1$ number of equations that were contributed from the $N$ number of Eq. (A.1) in Appendix A and one equation related to the surface boundary condition. The choice of trial function, Eq. (34), automatically ensures the symmetry boundary condition that the center of the particle is fulfilled at each instance in time. The same method was applied for the first and second derivatives of $T$, which directly transform the differential equation to algebraic form using the orthogonal coefficients, $A_{i,j}$ and $B_{i,j}$.

The orthogonal collocation method requires space variable to be converted into the dimensionless form, which represent 0 as the center point coordinate and 1 as the surface coordinate. The final form of the energy balance transformed into a system of ODEs is presented in Eq. (37).

$$\begin{aligned}\sum \rho_{k,j} Cp_{k,j} \frac{\partial T}{\partial t} &= \frac{\lambda_{eff,j}}{x^a R^2}\left(\alpha x\left(\sum_{i=1}^{N+1} A_{j,i} T_i\right) + x^a\left(\sum_{i=1}^{N+1} B_{j,i} T_i\right)\right) - \dot{r}_{v,gas,j} Cp_{g,j} \frac{V_p}{RA_p} \\ &\left(\sum_{i=1}^{N+1} A_{j,i} T_i\right) + \left(D_{fw,j} Cp_{fw,j}\left(\sum_{i=1}^{N+1} A_{j,i}\rho_{fw_i}\right) + D_{bw,j} Cp_{bw,j}\left(\sum_{i=1}^{N+1} A_{j,i}\rho_{bwi}\right)\right) \\ &\left(\sum_{i=1}^{N+1} A_{j,i} T_i\right) + \Delta H_{dry,j}\dot{r}_{v,dry,j} + \Delta H_{dev,j}\dot{r}_{v,dev,j}\end{aligned} \tag{37}$$

The transformation of the other equations must follow the transformation presented above, i.e. the space variable is dimensionless and replaces the derivative term with the orthogonal collocation coefficients. The coordinate of orthogonal collocation points is generated from the roots of the shifted Legendre orthogonal polynomial, which are summarized in Table B.1 in Appendix B.

### 2.4. Source term calculation

Biomass decomposition is a continuous process that proceeds from the particle surface towards the particle center at a rate determined by the propagation of the heat wave. The utilization of the orthogonal collocation method can be further improved to allow for the

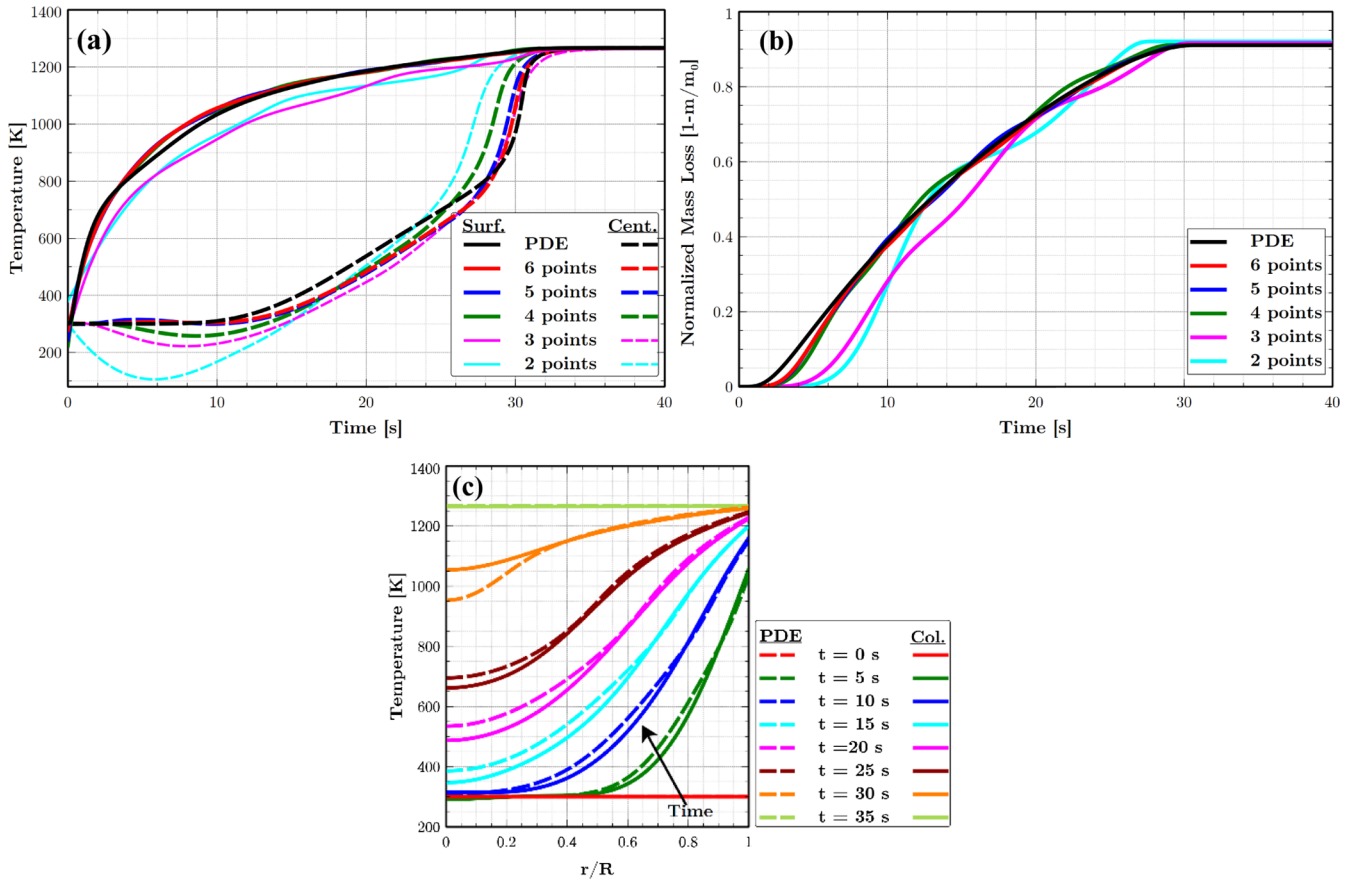


**Fig. 4.** Mesh independency test for simulation using 9.5 mm diameter spherical particle, (a) temperature profile (b) normalized mass loss profile for different collocation point simulations (c) simulation of temperature history comparison through particle radius between PDE solver and six collocation points.

propagation of the reactions throughout the biomass particle at and in between the collocation points. This relies on expanding the coverage of source term calculation from only a collocation point to also account for the reaction that occur between collocation points. The calculation of the local reaction rate at each collocation point ($i$) is performed using the mass weighted averaging reaction rate on the expansion points over adjacent Euclidean points, $(j+1)$ and $(j-1)$. The mass weighting average of a reaction rate follows Eq. (38). ($k$ = reaction and components index, $i$ = collocation points index, $j$ = Euclidean points index, and $l$ = expansion points index)

$$\bar{\dot{r}}_{v,k,i} = \frac{\int_{rj-1}^{rj+1} A_{k,l}\exp\left(-\frac{E_{ak,l}}{R_g T_l}\right)\times\rho_{k,l}\times A_{layer,l}\,dr}{\int_{rj-1}^{rj+1}\rho_{k,l}\times A_{layer,l}\,dr}\times\rho_i \tag{38}$$

where $A_{layer,j}$ is the perpendicular area of the specific layer (for spherical geometry, $A_{layer,j} = 4\pi r^2$, while for cylindrical and planar it is calculated as $2\pi r L_p$ and $L_p \times W_p$). The properties of each expansion point, i.e. temperature and density, are calculated to determine a high resolution profile for the reaction rates. The temperature at each expansion point is easily determined from the orthogonal collocation coefficients that are obtained at each time step, while the local density is interpolated using piecewise cubic hermite polynomials, which has been proven to provide a good solution in the sub-grid-scale interpolation of reaction source terms [56].

## 3. Model assessment

MATLAB 2016b ® was used to simulate the resulting system of coupled algebraic-differential equations, specifically the built-in ODE solver (ode15s). For the purpose of validating the accuracy of the orthogonal collocation method, the partial differential equations were solved directly with the built-in PDE solver (pdepe). This allowed the validation of the numerical discretization method with respect to the essential physicochemical phenomena, including drying, propagation of heat wave, and reaction source terms. The numerical accuracy test was performed by comparing the simulation results at conditions relevant to the experimental results performed by other researchers. The list of experiments and corresponding operating conditions is summarized in Table 5.

The biomass material data and characteristics used in the present experimental work were the main criteria for the selection of the correct properties. The data in Table C1 in Appendix C was used for the biomass particle simulations herein.

Two different devolatilization kinetic schemes were employed in this study for different purposes. The one-step global mechanism, which has no competitive reactions, was used to confirm mesh independence, i.e. to validate the number of colocation points needed for the solution to converge with the high resolution mesh-based method. Meanwhile, a kinetic scheme with three independent competitive reactions was used to validate the model with pyrolysis and combustion experiments. The utilization of that scheme followed the recommendation from the original experiment paper [12] even though the employed kinetic was originally derived from pine wood instead of poplar wood [57]. The activation energies, pre-exponential factors, and the heat of reaction used in the present study are summarized in Table C2 in Appendix C.

### 3.1. Grid independence

A grid-independent study was necessary to assess the accuracy of the numerical discretization scheme and to determine the optimal use of collocation points. Finding an optimal number of collocation points is crucial in order to avoid unnecessary and excessive usage that produce no significant improvements. The grid-independent study herein was performed by comparing the simulation results of surface temperature, center temperature, and mass evolution, using different numbers of collocation points, i.e. from two to six points, as presented in Fig. 4a and b. The results obtained from the PDE solver are also presented here as a benchmark of the true solution, as it relies on employing 200 computational grid points.

Significant improvements were obtained with the addition of more collocation points up to 4 points, while 5–6 points produced almost similar results, as shown in Fig. 4a and b. The more colocation points employed, the closer agreement result obtained with the PDE solver. Utilization of six collocation points produced the highest degree of agreement with the PDE results in terms of spatial temperature history at the center point, as presented in Fig. 4c. It can be concluded that four collocation points is the optimum number to produce the mesh independent result for 9.5 mm diameter spherical particle simulation, as used in model validation cases. However, six collocation points were used for the rest of the analysis, which gives a margin for simulating kinetics with higher activation energies that cause narrower reaction zones inside the particle. Efficiency was maintained since the computational time did not increase drastically using six collocation points.

### 3.2. Source term evaluation

This section presents comparisons of simulation results with and without improved resolution of reaction rate using the mass weighted average method in Eq. (38). Two different kinetics schemes and kinetics parameters were employed. Fig. 5a shows the results for calculations with and without improved resolution using the global kinetic scheme or the reaction index 0 in Table C2, using 9.5 mm diameter spherical particle. Fig. 5b shows three independent parallel reaction schemes, or

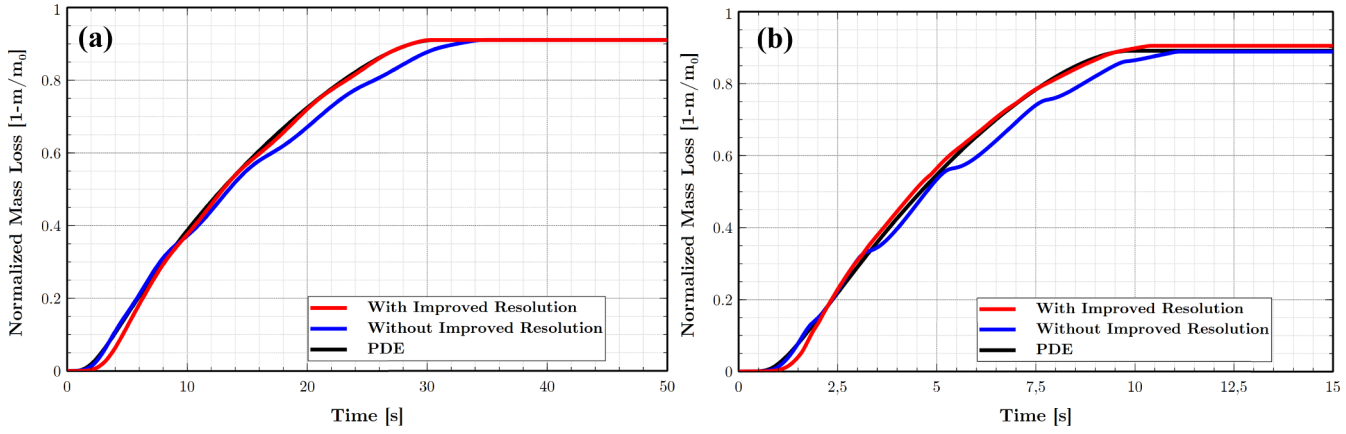


**Fig. 5.** Normalized mass loss results with and without improved resolution of reaction rate using Eq. (38) (a) with global kinetic scheme (low activation energy) and (b) three parallel independent reaction schemes (high activation energy).

reaction indexes 1 to 3, with 5 mm diameter spherical particle.

The mass evolution results without improved resolution simulation are observed to be less smooth profile, as presented in Fig. 5a and even worse in Fig. 5b. This was due to the much higher activation energy. Less smooth behaviors are observed due to the wide distance of each collocation point to cover a very narrow reaction rate band. The less smooth profile became very prominent when the devolatilization reached the inner collocation points where the distance between the points was wider.

Discretization by orthogonal collocation does not automatically calculate the reaction that occurs between collocation points. This may produce sudden changes in mass loss derivative when the reaction occurs very fast at one collocation point but the temperature is not sufficient to start the reaction at the next inner point. This effect was found to be more prominent in higher activation energy. The problem can be solved by employing more collocation points, which would consequently increase the computational effort.

An alternative used in this work with an insignificant increase in computational effort expands the coverage of reaction area and calculates the mass weighted reaction rate following Eq. (38). Based on Fig. 5, the results without improved resolution provide worse agreement with the results from PDE solver compared to the results with improved resolution. This method was proven to diminish the less smooth profile in the mass loss profile and simultaneously improve the accuracy of the prediction, by better agreement with the results from PDE solver. This analysis also shows the applicability of the combination of the orthogonal collocation method with the current improved resolution method for any arbitrary kinetic reaction, i.e. for the complete range of activation energy found in the literature.

### 3.3. Influence of moving coordinates

The accumulation term on the left side of Eq. (2) should be revised due the transformation of the space variable into the dimensionless form. The revision of the accumulation term was needed during particle shrinking since the space variable is bounded between 0 and 1, even when the physical dimension changes in time due to char reaction, i.e. particle radius, $R = f(t)$. This adjustment was necessary otherwise the interpretation of local temperature in the updated coordinate became inaccurate. The revision of the accumulation term follows Eq. (39), and in the discretized form by orthogonal collocation follows Eq. (40).

$$\sum \rho_k Cp_k \left( \frac{\partial T}{\partial t} + \frac{1}{R} \frac{\partial T}{\partial x} \frac{\partial R}{\partial t} \right) \tag{39}$$

$$\sum \rho_k Cp_k \left( \frac{\partial T}{\partial t} + \frac{1}{R} \left( \sum_{j=1}^{N} A_{i,j} T_j \right) \frac{\partial R}{\partial t} \right) \tag{40}$$

The importance of including the moving coordinate term in shrinking particle modelling is presented in Fig. 6. This figure summarizes the simulation result for the particle combustion with and without a moving coordinate. The inclusion of a moving coordinate term produced a slightly faster prediction of mass loss, as expected. Without the inclusion of a moving coordinate, the fix coordinate would receive the wrong properties, which would slightly underestimate heat transport and, consequently, predict slower particle combustion.

The difference is insignificant considering the very minor difference in predicted mass and radius evolution, as shown in Fig. 6a. This finding is due to the small temperature gradient seen when the particle started to shrink. In Eq. (39), the $\partial T/\partial x$ term cancelled the $\partial R/\partial t$ term, which produced an insignificant change in temperature and the prediction of mass evolution for simulations with and without a moving coordinate. This effect was neglected in the present study.

In a larger particle and/or faster heating rate in combustion simulation, the effect of a moving coordinate is small but not negligible, as reflected in Fig. 6b for the case of simulation of a 20 mm diameter particle. The larger temperature gradient was seen when shrinking started to occur in the bigger particle, which caused the effect of moving coordinate term inclusion become prominent.

### 3.4. Effect of Stefan flow

The Stefan flow adds a convective transport to or from the surface depending on the net molar flow at the surface. As a consequence of this, both convective mass and heat transport should be corrected by considering the net outflow of the Stefan flow and penetrating bulk gas. It is assumed the material is isotropic allowing an even flow of gas through the boundary layer, while in reality the flow can be larger in the fiber direction and also effected by intermittent bursts due to cracks in the material. The gases emitted from the particle, the Stefan flow, had a large effect on mass and heat transfer. As presented in Fig. 7, the Stefan flow had a significant effect on the global prediction of mass and radius evolution.

The effect of Stefan flow on convective heat flux was found to be very minor during the first five seconds of simulation, before any major char reaction had occurred. During this period, a high amount of gas emitted from the particle surface was found. The difference is small because the radiative heat transport from wall to particle is not affected by Stefan flow. The influence of Stefan flow is not significant since 95% of the total heat transfer to the particle is due to radiative heat transfer and only 5% is due to convective heat transfer.

A major discrepancy began when the particle surface reached the char reaction temperature (about 800 K). At this point, t greater than 5 s, the effect of the Stefan flow hindered the oxidative gas from penetrating into the particle surface boundary layer. This obstacle reduced the mass transfer rate, thereby lowering the char reaction rate. Since the exothermic char reaction has almost the same contribution as

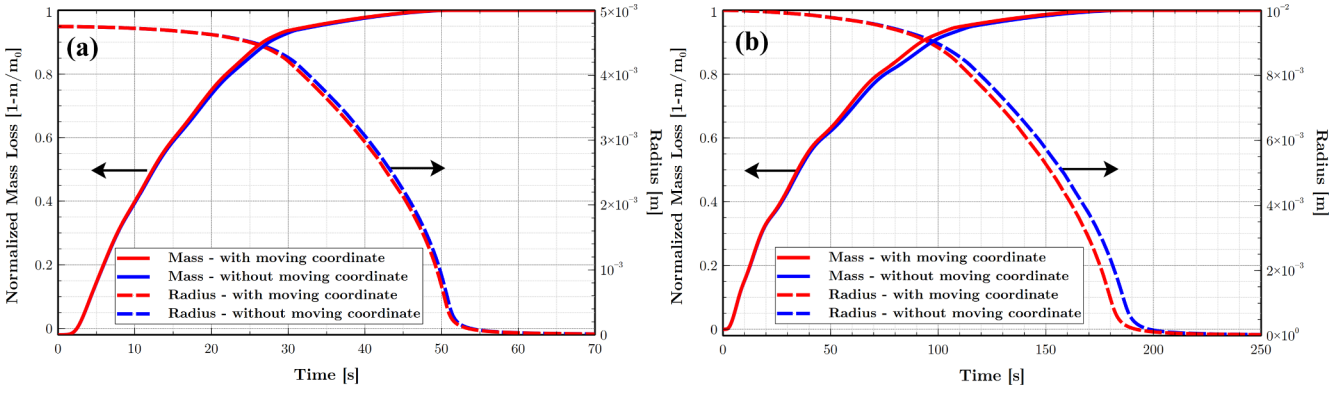


**Fig. 6.** Comparison of normalized mass loss and radius evolution results between simulation with and without moving coordinate term (a) using 9.5 mm diameter (b) using 20 mm diameter.

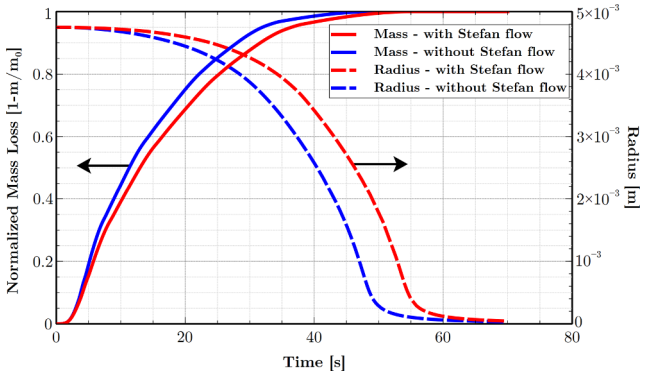


**Fig. 7.** Comparison of normalized mass loss and radius evolution results between simulations with and without the Stefan flow effect for 9.5 mm diameter spherical particle combustion.

radiation heat for heat flux in particle surface, the reduction in char reaction rate has a major impact on the total heat and mass balances. This occurred until the Stefan flow diminished at around 40 s, as shown in Fig. 7. In terms of global prediction, the Stefan flow caused a significant effect during an intermediate time interval and cannot be omitted from the analysis.

## 4. Results and discussion

This section discusses the results of validations of simulations of inert and reactive conditions that qualitatively and quantitatively describe the advantage of orthogonal collocation for particle modelling purposes, in terms of numerical accuracy and efficiency. The accuracy of the orthogonal collocation method was evaluated by comparisons with the pyrolysis and combustion experiments for single biomass particles reported by Lu et al. [12]. The comparisons with previous simulations that rely on both mesh-based models (Lu et al. [12] and Haberle et al. [15]) and interface-based models (Ström & Thunnman [17], Mehrabian et al. [21], and Gomez et al. [24]) is also presented.

### 4.1. Biomass pyrolysis

A comparison of the present simulation results with the pyrolysis experiment is shown in Fig. 8a–d. Particle surface temperature, particle center temperature, and mass evolution during conversion were selected as the criteria to determine the agreement between simulation and experimental findings. The three validation cases (A to C) have different features in terms of shapes and initial moisture content, which allows a test of the stability and accuracy of the physicochemical model and discretization scheme in simulating various conditions of biomass pyrolysis.

Fig. 8a shows the simulation results of mass evolution, which produced overall good agreement with the experimental data. The mass loss evolution of different particle characteristics, including geometry and moisture content, were predicted in a correct manner. The dry spherical particle displayed a faster mass reduction than the dry cylindrical particle and the wet cylindrical particle. Both dry particles leveled out at a lower value of mass loss than the moist particle, as expected.

The predicted particle center and surface temperatures were also in good agreement with the experimental data, as shown in Fig. 8b, c, and d. The different stages of particle decomposition can be seen in the temperature profiles. The drying phase, which occurred around 373 K, is clearly seen in the wet particle simulation in Fig. 8d. The center temperature plateau is obtained for about half period of experiment when the endothermic drying occurred. After that, the center

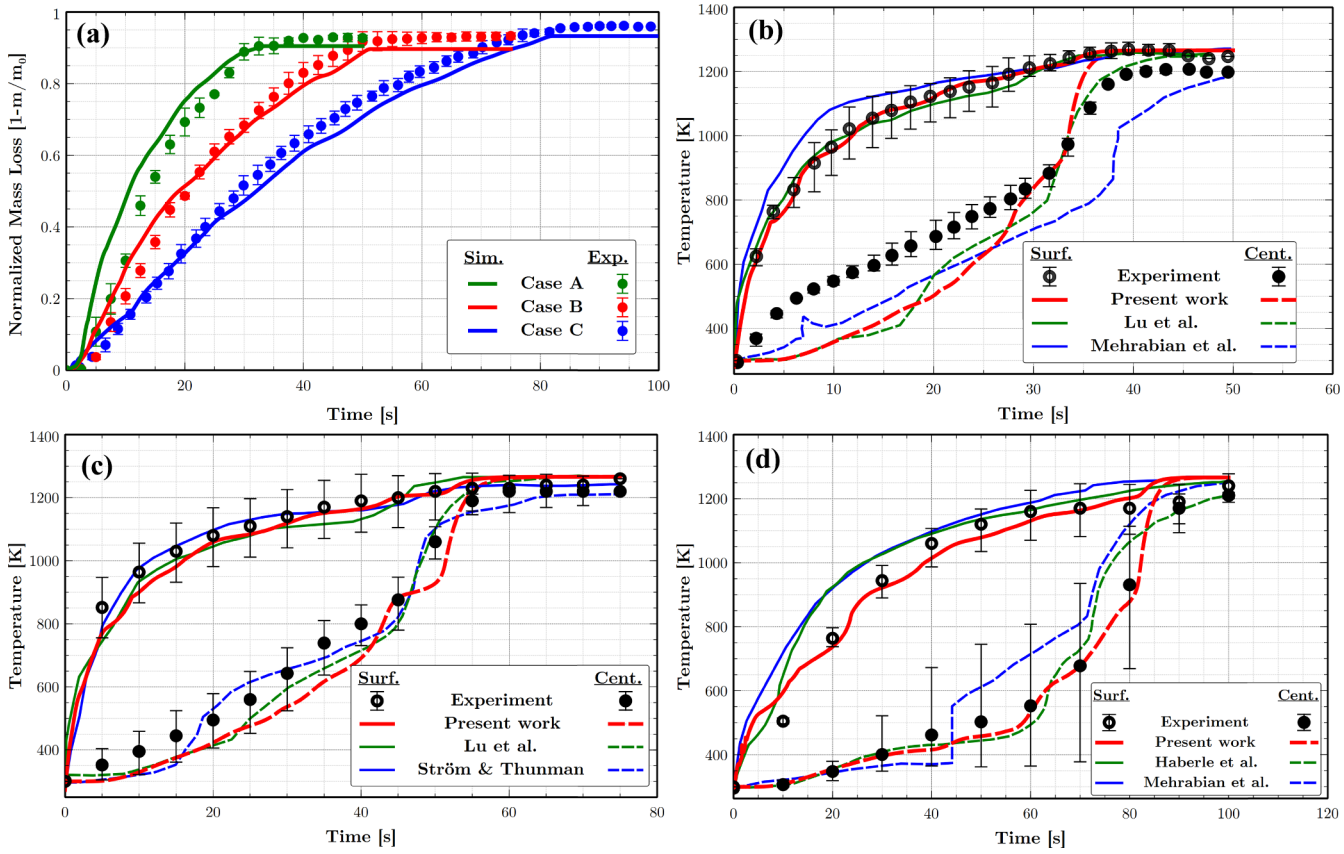


**Fig. 8.** Comparison between simulated and measured (a) normalized mass loss of Case A, B and C, (b) temperature for Case A experimental data with error bars, (c) temperature for Case B, and (d) temperature for Case C (red : orthogonal collocation based-model, blue: interface-based model, green: mesh-based model).

temperature started to increase up to the devolatilization temperature around 500 K before decreasing. The endothermic devolatilization hindered the temperature from increasing during this period until all dry biomass had converted into volatile gas, tar, and solid char. The devolatilization was completely finished at about 900 K, at which point the center temperature slope started to increase again and leveled out slightly below the wall temperature, i.e. higher than the bulk gas temperature due to the effect of the transfer of radiative heat transfer from the walls.

A discrepancy was found in the prediction of the center temperature in the dry spherical particle simulation in Fig. 8b. The center temperature in Fig. 8b is increased faster than in Fig. 8c–d, which is not reasonable. The center temperature increase must also be limited by the time constant for heat diffusivity from a theoretical point of view. The original experimental study [12] also described the issue of measuring the center temperature of a spherical particle in an accurate way. Lateral heat conduction from the outer parts of the thermocouple is believed to have caused the faster increase in the temperature at the center.

Another discrepancy was found in the simulation of the surface temperature of wet cylindrical particle, in Fig. 8d. The surface temperature of all simulations works, i.e. collocation, mesh-based and interface-based models, are increased faster during the first 10 s compared to the experimental result. In the later phase from 10 s until the final stage, the collocation method provided best agreement which might be related to inclusion of different physical phenomena in the model. The evolution of the surface temperature was smooth in all cases except for the case with high moisture content which showed minor fluctuations. However the interior points and the center point showed smooth temperature profiles for all cases. The stability was also proven by the smooth particle conversion profiles for all validation cases in Fig. 8a. This confirmed stable temperature evolution in the zones where evaporation and devolatilization reactions occurred. Moreover, the particle conversion was observed to be very stable as presented by stable reaction rates over the entire simulation time in Fig. 9.

The mesh-based model is the most sophisticated model and is expected to produce more accurate results because it uses many more computational grids than the orthogonal collocation-based model and the interface-based model. However, the comparison provided in Fig. 8b to d indicates that simulation accuracy can be maintained by using the orthogonal collocation method. The comparison with previous simulations lead to the conclusion that the current simulation produced almost similar temperature prediction with the mesh-based and the interface-based simulation works. These results are promising considering that the present study does not rely on tuning parameters, nor does it require the specification of surface boundary conditions as in studies that rely on the interfaced-based model. Notably, the experimental uncertainties for temperature measurements were fairly large as indicated by the large error bars which makes it difficult to judge which of the models agrees best.

Analysis of the reaction rate distribution inside the particle reveals that reactions occur in a narrow region. Fig. 9 shows that the reaction zones are distributed initially around 5% and, at later stages, up to 20% of the particle radius. This wide range of devolatilization reaction zones was found especially in the early phase of the devolatilization stage when the temperature had not exceeded 700 K. The Pyrolysis number at this stage was found to be much more than 1, which physically indicates that the reaction proceeded slower than the temperature wave [58]. In the higher temperature region, the Pyrolysis number shifted to lower than 1, which implies the applicability of sharp interface models in that region.

### 4.2. Biomass combustion

The simulation results from the particle combustion case are presented in Fig. 10a and b. The results of surface temperature, center temperature, and normalized mass loss as a function of time are shown as a comparison with experimental data in Fig. 10. Normalized mass loss prediction from simulation, produces a very good agreement with the experimental data.

Similar to previous findings, discrepancies were found for the center and surface temperatures, as shown in Fig. 10a. As discussed in the original paper [12], the surface thermocouple did not measure the correct temperature because the particle had started to shrink while the thermocouple remained in its fixed position. The surface thermocouple measured the gases around the particle instead of the particle surface when the particle started to shrink and it was influenced by the transfer of radiative heat from the walls.

Both experimental data and simulation results displayed the same phenomena during the final period of char reaction. Particle temperature increased gradually up to the peak point and sharply declined as no char was left in the particle. This is explained by the effective kinetic rate for char reaction, which increases sharply during particle radius reduction. The reduction of particle diameter influence on the increasing of convective mass transport coefficient in Eq. (20). Once the char had been consumed completely, the temperature cooled down because the bulk gas cooled since no particle remained. This final temperature fell quickly when the particle was completely burnt at around 85 s, which is consistent with the mass evolution in Fig. 10b.

Comparison with previous simulations revealed that the mesh-based simulation results from Lu et al, which exclude the effect of the flame in the gas phase, produced similar results as the collocation method simulation which also exclude the presence of flame (red line in Fig. 10). Meanwhile, the interface-based model simulation by Mehrabian et al. and Gomez et al., which include the flame due to combustion in the gas phase using CFD simulation, predicted higher temperature closer to experimental data in the later phase. It is noted that experimental errors are larger for temperature compared to mass evolution due to the experimental setup. It is clear that the measured surface temperature is higher than all simulations in the early phase which is probably due to that thermocouple detached from the particle surface when particle started to shrink, as explained by Lu et al. [12]. It is likely that he surface thermocouple was measuring gas combustion temperature instead of surface temperature. Better prediction of global mass and temperature prediction was observed in Fig. 10 (purple line) by the inclusion of radiation from flame due to combustion in the gas phase. The radiative heat source was added in the heat balance at boundary condition in Eq. (3) by assuming the flame temperature to be 2000 K and gas emissivity was about 0.2. This illustrates the importance of handling the boundary condition carefully and that it has a significant effect on the thermochemical degradation of the biomass particle [14].

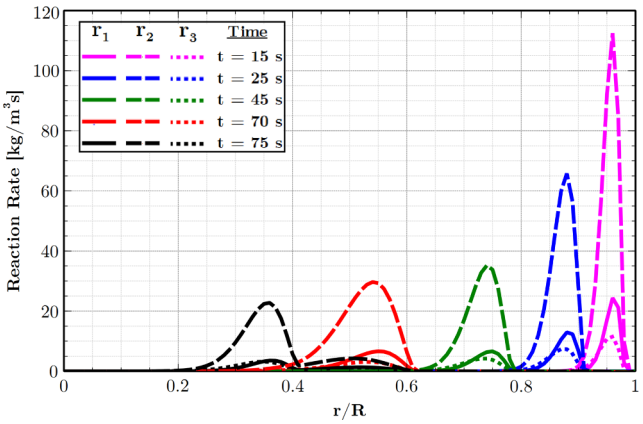


**Fig. 9.** Simulation history of devolatilization reaction rate over particle radius (indexes 1, 2, and 3 refer to kinetics in Fig. 3b).

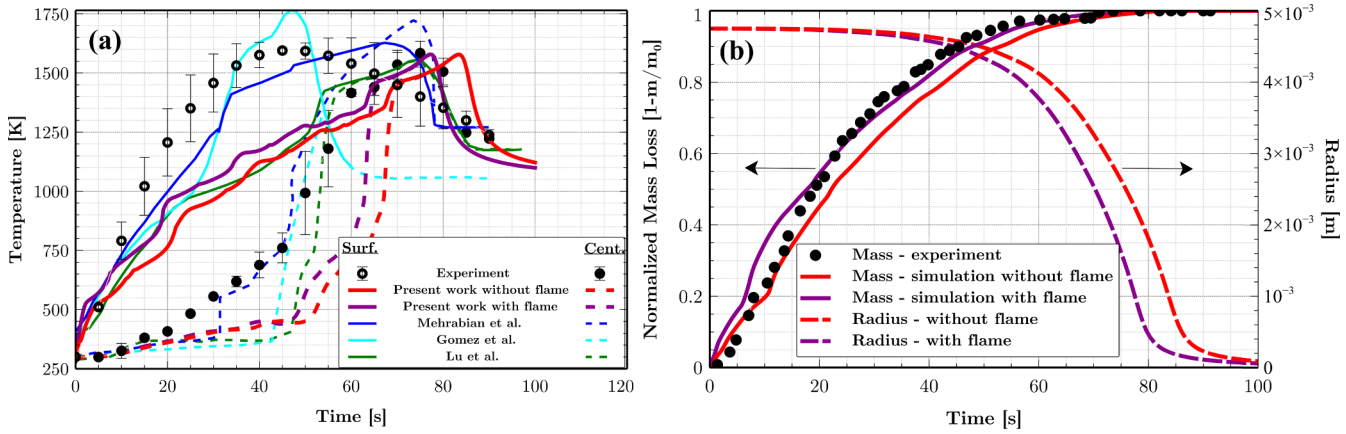


**Fig. 10.** Comparison between simulation results and experimental data from Case D, (a) temperature profiles (b) normalized mass loss and radius evolution (red & purple: orthogonal collocation based-model, blue & cyan: interface-based model, green: mesh-based model).

### *4.3. Computational efficiency*

The simulation time was recorded and compared with other simulation works to give guidance on the cost of implementing the new particle model. The recording of simulation time is an important factor in judging if the particle model can be implemented as sub-grid functions in a CFD analysis. The simulation time in the present study depends on the number of collocation points and is currently in the order of seconds, but the time can be further improved by code optimization and compilation.

A previous study using the mesh-based discretization method reported that at least 2930 s (48 min) were required to simulate experimental Case C [15]. The results indicate approximately three orders of magnitude faster simulations, while similar accuracy was maintained. The simulation time for the combustion case (Case D) increased only 20% compared to the simulation time for particle pyrolysis with the same level of initial moisture content (Case C). It is challenging to compare the efficiency of different simulation methods, due to differences in model formulation, hardware and software used. However it is not controversial to conclude the current simulation method is more efficient compared to mesh-based simulations methods as it has been demonstrated to predict both combustion and pyrolysis accurately with six collocation points. Optimization of the code allows even more efficient simulation. For example the computational efficiency can be improved by utilizing MEX-files in the Matlab solver which are dynamically loaded after being compiled. The authors showed that for systems of differential equations, the simulation time can be reduced by more than 80% by using MEX-files [59]. Another option is utilization of a more efficient ODE solver, for example CVODE. Studies by Gonnet et al. [60] showed this allows significant reduction of simulation time compared to the Matlab solver. The aforementioned solver was proven to work accurately and efficiently in the biomass particle pyrolysis application [61]. The short simulation time needed in the present study is very promising in that a single particle can be implemented in CFD analysis to describe a bed of particles, which allows full coupling with local gas flow and the temperature surrounding the particles.

## 5. Conclusion and recommendations

A new model for single particle pyrolysis and combustion was developed using the orthogonal colocation method. By abandoning the classical formulation for lumped models, i.e. interface-based models, the current approach allows decoupling between biomass components and spatial resolution and also the prediction of continuous intra-particle profiles. The discretization scheme combined with a comprehensive physicochemical particle model provides improvement in heat and mass transfer rates inside and at the particle surface. The model formulation also provides great flexibility, including the incorporation of (i) arbitrary reaction kinetics, (ii) local varying properties, (iii) heat adsorption by evaporated gas, (iv) gradient-driven transport mechanisms, such as water movement caused by diffusion inside the biomass matrix, and (v) inclusion of the effect of Stefan flow on the heat and mass transfer rates at the particle surface.

Model validation using data from particle pyrolysis and combustion experiments for different particle moisture contents and shapes confirmed that the intra-particle temperature gradient, as well as particle mass and size evolution, can be predicted accurately. Some minor discrepancies were found, and these are believed to be due to uncertainties in the experimental measurements. Good results were related to accurate intra-particle resolution i.e. the prediction of continuous profiles including temperature and the finite reaction zones. The reaction zone was found to be approximately 5% of the particle radius in the early stage, whereas it increased up to 20% of the radius later in the process. Six collocation points were found to be sufficient to provide enough resolution for the particles used in pyrolysis and combustion experiments. However, a few more collocation points might be required to provide the same high degree of accuracy if the model is used for much larger particles.

The importance of including different physical phenomena in the model was examined. Results showed that Stefan flow has a significant influence on predicted mass loss and radius evolution but only for a limited time. The largest effect of Stefan flow was found in an intermediate time window. This is because radiation dominates the rate of convective heat transfer in the early phase, while the rate of oxygen mass transfer is less influenced when the counter-current flow of the devolatilization gas is negligible when only char remains in the later phase of combustion. It was found that the inclusion of a moving coordinate term is not important for the systems studied. However, this term might need to be included in the combustion of very large particles or processes with much faster heating.

The comparisons with previous simulation studies, including mesh-based and interface-based ones, are also provided. It was found that the model allows equally good results as mesh-based simulation, however with the advantage of being computationally more efficient and

possible to implement as sub-grid models in CFD as a system of coupled ordinary differential equations. The present results were equally as good as those obtained using interface-based models. The present model is considered to be a significant contribution, as it requires neither tunable model parameters nor the specification of particle surface boundary conditions from experiments. These are instead calculated explicitly from the balance equations at the particle interface. The proposed discretization method also allows implementation of more complex reaction scheme and inclusion of char gasification reaction inside the particle by modeling the transport of the pyrolytic gas inside the particle. These results, thereby, confirm the ability of current particle model to accurately and efficiently simulate particle pyrolysis and combustion.

**Acknowledgements**

Financial support from the Swedish Research Council (Grant: 348-2014-3522) is gratefully acknowledged.

## Appendix A. – Derivation of orthogonal collocation equation

Solving for all collocation points for Eq. (34) produces a matrix that can be represented as:

$$T = Qd$$

The solution of $d$ follows:

$$d = Q^{-1}T$$

Substituting the $d$ value into the expanded solution at each collocation point in Eq. (34) gives :

$$T(x_j) = \left(\sum_{i=1}^{N+1} x_j^{2i-2}\right) Q^{-1}T \tag{A.1}$$

The same derivation can be applied for the first and second derivative equation, which gives the matrix form solution for all collocation points as follows:

$$\frac{dT}{dx} = Cd \text{and} \frac{d^2T}{dx^2} = Dd$$

Solving for $d$ and substitution into the expansion solution at each collocation point produced:

$$\frac{dT}{dx}(x_j) = AT \text{and} \frac{d^2T}{dx^2}(x_j) = BT$$

The orthogonal collocation solution requires that the space variable is converted into dimensionless space, as presented in these expressions:

$$r = xR; \frac{\partial T}{\partial r} = \frac{1}{R}\frac{\partial T}{\partial x}; \frac{d^2T}{dr^2} = \frac{1}{R^2}\frac{d^2T}{dx^2}$$

## Appendix B. – Collocation points coordinate

(See Table B1)

**Table B.1**
The collocation point locations for different geometries (planar, cylindrical, and spherical).

| N | Geometry | | |
|---|---|---|---|
| | Planar | Cylindrical | Spherical |
| 1 | 0.57735 02692 | 0.70710 67812 | 0.77459 66692 |
| 2 | 0.33998 10436 | 0.45970 08434 | 0.53846 93101 |
| | 0.86113 63116 | 0.88807 38340 | 0.90617 93459 |
| 3 | 0.23861 91861 | 0.33571 06870 | 0.40584 51514 |
| | 0.66120 93865 | 0.70710 67812 | 0.74153 11856 |
| | 0.93246 95142 | 0.94196 51451 | 0.94910 79123 |
| 4 | 0.18343 46425 | 0.26349 92300 | 0.32425 34234 |
| | 0.52553 24099 | 0.57446 45143 | 0.61337 14327 |
| | 0.79666 64774 | 0.81852 94874 | 0.83603 11073 |
| | 0.96028 98565 | 0.96465 96062 | 0.96816 02395 |
| 5 | 0.14887 43390 | 0.21658 73427 | 0.26954 31560 |
| | 0.43339 53941 | 0.48038 04169 | 0.51909 61292 |
| | 0.67940 95683 | 0.70710 67812 | 0.73015 20056 |
| | 0.86506 33667 | 0.87706 02346 | 0.88706 25998 |
| | 0.97390 65285 | 0.97626 32447 | 0.97822 86581 |

## Appendix C. – Supporting data for simulation

(See Tables C1 and C2)

**Table C1**
Simulation and particle properties.

| Property | Value |
|---|---|
| True biomass density ($\rho_{tot,true}$) [62] | 1500 |
| Oven dry biomass density, 20% moisture ($\rho_{tot}$) [62] | 359 |
| Initial porosity ($\varepsilon$) [12] | |
| Poplar (6%wt moisture) | 0.74 |
| Poplar (40%wt moisture) | 0.60 |
| Initial ash content [63] | 1.0 |
| Particle pore diameter ($d_{pore}$) [12] | $3.2\times10^{-6}$ |
| Thermal conductivity for : | |
| Wet biomass ($\lambda_b$) [12,64] | $(0.129 + 4.9\times10^{-2}C_m)(1 + (2.05 + 4C_m)\times10^{-3}(T - 273.15))(0.986 + 2.695C_m)$ where: $C_m = \frac{\rho_b + \rho_{fw} + \rho_{bw}}{\rho_{tot}}$ |
| Char ($\lambda_c$) [21,65] | $1.47 + 1.1\times10^{-3}T$ |
| Ash ($\lambda_{ash}$)[12] | 1.2 |
| Gas ($\lambda_g$) [66] | $0.0109 + 6.0\times10^{-5}T$ |
| Heat capacity for : | |
| Dry biomass ($Cp_b$) [21] | $1500 + T$ |
| Free water ($Cp_{fw}$) [66] | 4200 |
| Bound water ($Cp_{bw}$) [66] | 4200 |
| Char ($Cp_c$) [21] | 1700 |
| Ash ($Cp_{ash}$) [14] | $754 + 0.586\times(T - 273)$ |
| Emissivity for : | |
| Dry biomass($\omega_b$) [12] | 0.85 |
| Char ($\omega_c$) [12] | 0.95 |
| Ash ($\omega_{ash}$) [12] | 0.7 |
| Bulk gas velocity* | 0.1 |

* estimated value, due to lack of information from original paper [12].

**Table C2**
Kinetic rate data.

| Reaction Index | Reaction | A ($s^{-1}$) | Ea (kJ $mol^{-1}$) | ΔH (kJ $kg^{-1}$) |
|---|---|---|---|---|
| One step global scheme: [51] | | | | |
| 0 | Dry biomass → 0.46 Gas + 0.46 Tar + 0.08 Char | $7.41\times10^{4}$ | 83.6 | 150 |
| Three independent competitive reactions scheme : | | | | |
| 1 | Dry biomass → Gas [12] | $1.11\times10^{11}$ | 177 | 418 |
| 2 | Dry biomass → Tar [12] | $9.28\times10^{9}$ | 149 | 418 |
| 3 | Dry biomass → Char [12] | $3.05\times10^{7}$ | 125 | 418 |
| Char oxidation and gasification: | | | | |
| 4 | $C + O_2 \rightarrow CO_2$ [12] | $0.658\ T$ (m $s^{-1}$) | 74.8 | −32,000 |
| 5 | $C + CO_2 \rightarrow 2CO$ [12] | $3.42\ T$ (m $s^{-1}$) | 130 | 14,370 |
| 6 | $C + H_2O \rightarrow CO + H_2$ [12] | $3.42\ T$ (m $s^{-1}$) | 130 | 10,940 |
| Water drying : | | | | |
| 7 | $H_2O$ (l, free) → $H_2O$ (g) [15] | $5.13\times10^{8}$ | 88 | 2440 |
| 8 | $H_2O$ (l, bound) → $H_2O$ (g) [15] | $5.13\times10^{8}$ | 88 | 2440 |

## References


[1] Zhao P, Shen Y, Ge S, Chen Z, Yoshikawa K. Clean solid biofuel production from high moisture content waste biomass employing hydrothermal treatment. Appl Energy 2014;131:345–67.
[2] Porteous A. Energy from waste: a wholly acceptable waste-management solution. Appl Energy 1997;58:177–208.
[3] Roy MM, Corscadden KW. An experimental study of combustion and emissions of biomass briquettes in a domestic wood stove. Appl Energy 2012;99:206–12.
[4] Yin C, Yan J. Oxy-fuel combustion of pulverized fuels: combustion fundamentals and modeling. Appl Energy 2016;162:742–62.
[5] Holtmeyer ML, Kumfer BM, Axelbaum RL. Effects of biomass particle size during cofiring under air-fired and oxyfuel conditions. Appl Energy 2012;93:606–13.
[6] Rezaei H, Sokhansanj S, Bi X, Lim CJ, Lau A. A numerical and experimental study on fast pyrolysis of single woody biomass particles. Appl Energy 2017;198:320–31.
[7] Ström H, Thunman H. A computationally efficient particle submodel for CFD-simulations of fixed-bed conversion. Appl Energy 2013;112:808–17.
[8] Di Blasi C. Heat, momentum and mass transport through a shrinking biomass particle exposed to thermal radiation. Chem Eng Sci 1996;51:1121–32.
[9] Bryden KM, Ragland KW, Rutland CJ. Modeling thermally thick pyrolysis of wood. Biomass Bioenergy 2002;22:41–53.
[10] Wurzenberger JC, Wallner S, Raupenstrauch H, Khinast JG. Thermal conversion of biomass: Comprehensive reactor and particle modeling. AIChE J 2002;48:2398–411.
[11] Grønli MG, Melaaen MC. Mathematical model for wood pyrolysis comparison of experimental measurements with model predictions. Energy Fuels 2000;14:791–800.
[12] Lu H, Robert W, Peirce G, Ripa B, Baxter LL. Comprehensive study of biomass particle combustion. Energy Fuels 2008;22:2826–39.
[13] Sand U, Sandberg J, Larfeldt J, Bel Fdhila R. Numerical prediction of the transport and pyrolysis in the interior and surrounding of dry and wet wood log. Appl Energy 2008;85:1208–24.
[14] Haberle I, Haugen NEL, Skreiberg Ø. Combustion of thermally thick wood particles: a study on the influence of wood particle size on the combustion behavior. Energy Fuels 2018;32:6847–62.
[15] Haberle I, Haugen NEL, Skreiberg Ø. Drying of thermally thick wood particles: a study of the numerical efficiency, accuracy, and stability of common drying models. Energy Fuels 2017;31:13743–60.
[16] Thunman H, Leckner B, Niklasson F, Johnsson F. Combustion of wood particles – A

particle model for Eulerian calculations. Combust Flame 2002;129:30–46.
[17] Ström H, Thunman H. CFD simulations of biofuel bed conversion: a submodel for the drying and devolatilization of thermally thick wood particles. Combust Flame 2013;160:417–31.
[18] Porteiro J, Granada E, Collazo J, Patino D, Moran JC. A model for the combustion of large particles of densitied wood. Energy Fuels 2007;21:3151–9.
[19] Porteiro J, Míguez JL, Granada E, Moran JC. Mathematical modelling of the combustion of a single wood particle. Fuel Process Technol 2006;87:169–75.
[20] Haseli Y, Van Oijen JA, De Goey LPH. A simplified pyrolysis model of a biomass particle based on infinitesimally thin reaction front approximation. Energy Fuels 2012;26:3230–43.
[21] Mehrabian R, Zahirovic S, Scharler R, Obernberger I, Kleditzsch S, Wirtz S, et al. A CFD model for thermal conversion of thermally thick biomass particles. Fuel Process Technol 2012;95:96–108.
[22] Gómez MA, Porteiro J, De la Cuesta D, Patiño D, Míguez JL. Dynamic simulation of a biomass domestic boiler under thermally thick considerations. Energy Convers Manage 2017;140:260–72.
[23] Haberle I, Skreiberg Ø, Łazar J, Haugen NEL. Numerical models for thermochemical degradation of thermally thick woody biomass, and their application in domestic wood heating appliances and grate furnaces. Prog Energy Combust Sci 2017;63:204–52.
[24] Gómez MA, Porteiro J, Patiño D, Míguez JL. Fast-solving thermally thick model of biomass particles embedded in a CFD code for the simulation of fixed-bed burners. Energy Convers Manag 2015;105:30–44.
[25] Finlayson BA. Packed bed reactor analysis by orthogonal collocation. Chem Eng Sci 1971;26:1081–91.
[26] Carey GF, Finlayson BA. Orthogonal collocation on finite elements. Chem Eng Sci 1975;30:587–96.
[27] Segall NL, Macgregor JF, Wright JD. Collocation methods for solving packed bed reactor models with radial gradients. Can J Chem Eng 1984;62:808–17.
[28] Kaczmarski K, Mazzotti M, Storti G, Morbidelli M. Modeling fixed-bed adsorption columns through orthogonal collocations on moving finite elements. Comput Chem Eng 1997;21:641–60.
[29] Babu B, Sastry KK. Estimation of heat transfer parameters in a trickle-bed reactor using differential evolution and orthogonal collocation. Comput Chem Eng 1999;23:327–39.
[30] McKay G. Solution to the homogeneous surface diffusion model for batch adsorption systems using orthogonal collocation. Chem Eng J 2001;81:213–21.
[31] Skoneczny S, Cioch M. Modeling of continuous-flow bioreactors with a biofilm with the use of orthogonal collocation on finite elements. Chem Eng Commun 2018;205:1–18.
[32] Rahimpour MR, Iranshahi D, Pourazadi E, Paymooni K. Evaluation of optimum design parameters and operating conditions of axial- and radial-flow tubular naphtha reforming reactors, using the differential evolution method, considering catalyst deactivation. Energy Fuels 2011;25:762–72.
[33] Afshar Ebrahimi A, Ebrahim HA, Jamshidi E. Solving partial differential equations of gas-solid reactions by orthogonal collocation. Comput Chem Eng 2008;32:1746–59.
[34] Bryden KM, Hagge MJ. Modeling the combined impact of moisture and char shrinkage on the pyrolysis of a biomass particle☆. Fuel 2003;82:1633–44.
[35] Johansson A, Fyhr C, Rasmuson A. High temperature convective drying of wood chips with air and superheated steam. Int J Heat Mass Transf 1997;40:2843–58.
[36] Khodaei H, Yeoh GH, Guzzomi F, Porteiro J. A CFD-based comparative analysis of drying in various single biomass particles. Appl Therm Eng 2018;128:1062–73.
[37] Fatehi H, Bai XS. A comprehensive mathematical model for biomass combustion. Combust Sci Technol 2014;186:574–93.
[38] Ciuta S, Patuzzi F, Baratieri M, Castaldi MJ. Enthalpy changes during pyrolysis of biomass: Interpretation of intraparticle gas sampling. Appl Energy 2018;228:1985–93.
[39] Salmasi A, Shams M, Chernoray V. An experimental approach to thermochemical conversion of a fuel particle in a fluidized bed. Appl Energy 2018;228:524–34.
[40] Haseli Y, van Oijen JA, de Goey LPH. Modeling biomass particle pyrolysis with temperature-dependent heat of reactions. J Anal Appl Pyrolysis 2011;90:140–54.
[41] Hagge MJ, Bryden KM. Modeling the impact of shrinkage on the pyrolysis of dry biomass. Chem Eng Sci 2002;57:2811–23.
[42] Biswas AK, Umeki K. Simplification of devolatilization models for thermally-thick particles: differences between wood logs and pellets. Chem Eng J 2015;274:181–91.
[43] Ranzi E, Cuoci A, Faravelli T, Frassoldati A, Migliavacca G, Pierucci S, et al. Chemical kinetics of biomass pyrolysis. Energy Fuels 2008;22:4292–300.
[44] Moilanen A, Saviharju K, Harju T. Steam gasification reactivities of various fuel chars. Adv Thermochem Biomass Convers 1993:131–41.
[45] Di Blasi C. Combustion and gasification rates of lignocellulosic chars. Prog Energy Combust Sci 2009;35:121–40.
[46] Karlström O, Brink A, Hupa M. Biomass char nitrogen oxidation - Single particle model. Energy Fuels 2013;27:1410–8.
[47] Robinson AL, Buckley SG, Yang N, Baxter LL. Experimental measurements of the thermal conductivity of ash deposits: Part 2. Effects of sintering and deposit microstructure. Energy Fuels 2001;15:75–84.
[48] Robinson AL, Buckley SG, Baxter LL. Experimental measurements of the thermal conductivity of ash deposits: Part 1. Measurement technique. Energy Fuels 2001;15:66–74.
[49] Janse AMC, Westerhout RWJ, Prins W. Modelling of flash pyrolysis of a single wood particle. Chem Eng Process Process Intensif 2000;39:239–52.
[50] De Paiva Souza ME, Nebra SA. Heat and mass transfer model in wood chip drying. Wood Fiber Sci 1998;32:153–63.
[51] Grønli MG. A theoretical and experimental study of the thermal degradation of biomass. ITEV-rapport 1996:115; 1996.
[52] Whitaker S. Forced convection heat transfer correlations for flow in pipes, past flat plates, single spheres, and for flow in packed beds and tube bundles. AIChE J 1972;18:361–71.
[53] Michaelides EE. Particles, bubbles and drops – their motion, heat and mass transfer. World Scientific Publishing Co. Pte. Ltd.; 2006.
[54] Bu C, Leckner B, Chen X, Gómez-Barea A, Liu D, Pallarès D. Devolatilization of a single fuel particle in a fluidized bed under oxy-combustion conditions. Part B: Modeling and comparison with measurements. Combust Flame 2015;162:809–18.
[55] Finlayson BA. Nonlinear analysis in chemical engineering. McGraw-Hill; 1980.
[56] Kuenne G, Avdić A, Janicka J. Assessment of subgrid interpolation for the source term evaluation within premixed combustion simulations. Combust Flame 2017;178:225–56.
[57] Wagenaar BM, Prins W, van Swaaij WPM. Flash pyrolysis kinetics of pine wood. Fuel Process Technol 1993;36:291–8.
[58] Pyle DL, Zaror CA. Heat transfer and kinetics in the low temperature pyrolysis of solids. Chem Eng Sci 1984;39:147–58.
[59] Soltani S, Andersson R, Andersson B. The effect of exhaust gas composition on the kinetics of soot oxidation and diesel particulate filter regeneration. Fuel 2018;220:453–63.
[60] Gonnet P, Dimopoulos S, Widmer L, Stelling J. A specialized ODE integrator for the efficient computation of parameter sensitivities. BMC Syst Biol 2012;6.
[61] Anca-Couce A, Zobel N. Numerical analysis of a biomass pyrolysis particle model: Solution method optimized for the coupling to reactor models. Fuel 2012;97:80–8.
[62] Ross RJ, USDA Forest Service. FPL. Wood handbook : wood as an engineering material; 2010.
[63] Jin W, Singh K, Zondlo J. Pyrolysis kinetics of physical components of wood and wood-polymers using isoconversion method. Agriculture 2013;3:12–32.
[64] Ouelhazi N, Arnaud G, Fohr JP. A two-dimensional study of wood plank drying. The effect of gaseous pressure below boiling point. Transp Porous Media 1992;7:39–61.
[65] Hermansson S, Thunman H. CFD modelling of bed shrinkage and channelling in fixed-bed combustion. Combust Flame 2011;158:988–99.
[66] National Institute of Standards and Technology (NIST). Chemistry WebBook 2001. https://webbook.nist.gov/chemistry/ [accessed August 6, 2018].